

Complex Grey Matter Structure Segmentation in Brains via Deep Learning: Example of the Claustrum

Hongwei Li¹, Aurore Menegaux^{2,3}, Felix JB Bauerlein⁴, Suprosanna Shit¹,
Benita Schmitz-Koep³, Christian Sorg^{2,3}, Bjoern Menze¹ and
Dennis Hedderich^{2,3}

1. Department of Informatics, Technical University of Munich, Germany

2. TUM-NIC Neuroimaging Center, Munich, Germany

*3. Department of Neuroradiology, Klinikum rechts der Isar, Technical University of
Munich, Germany*

*4. Department of Molecular Structural Biology, Max Planck Institute of Biochemistry,
Germany*

*5. Department of Psychiatry, Klinikum rechts der Isar, Technical University of Munich,
Germany*

Abstract

Segmentation and parcellation of the brain has been widely performed on brain MRI using atlas-based methods. However, segmentation of the claustrum, a thin and sheet-like structure between insular cortex and putamen has not been amenable to automatized segmentation, thus limiting its investigation in larger imaging cohorts. Recently, deep-learning based approaches have been introduced for automated segmentation of brain structures, yielding great potential to overcome preexisting limitations. In the following, we present a multi-view deep-learning based approach to segment the claustrum in T1-weighted MRI scans. We trained and evaluated the proposed method on 181 manual bilateral claustrum annotations by an expert neuroradiologist serving as reference standard. Cross-validation experiments yielded median volumetric similarity, robust Hausdorff distance and Dice score of 93.3%, 1.41mm and 71.8% respectively which represents equal or superior segmentation performance compared to human intra-rater reliability. Leave-one-scanner-out evaluation showed good transfer-ability of the algorithm to images from unseen scanners, however at slightly inferior performance. Furthermore, we found that AI-based claustrum segmentation benefits from multi-view information and requires sample sizes of around 75 MRI scans in the training set. In conclusion, the developed algorithm has large poten-

tial in independent study cohorts and to facilitate MRI-based research of the human claustrum through automated segmentation. The software and models of our method are made publicly available ¹.

Keywords: Claustrum, Image Segmentation, Deep Learning, Multi-view

1. Introduction

Parcellating the brain based on structural MRI has been widely performed in the last decades and has advanced our knowledge about brain organization and function immensely (Eickhoff et al., 2018; Arrigo et al., 2017; Bijsterbosch et al., 2018). In practice, the most established way to perform brain segmentation based on MRI, relies on atlas-based approaches after preprocessing and spatial normalization of an individual brain scan. Several atlases exist in standard space assigning distinct labels to specific brain structures either volume-based or surface-based (Desikan et al., 2006; Makris et al., 2006; Frazier et al., 2005). Atlas-based segmentation of a particular brain structure can then be used to explore its structural and functional connectivity using advanced MRI techniques in healthy cohort and patient populations (Goodkind et al., 2015; Arrigo et al., 2017; Glasser et al., 2016).

In the last decades, the study of brain structure on MRI has led to a lot of insights about distinct brain regions as well in physiologic and in pathologic conditions. Specifically, the exact determination of the volume and the extent of e.g. a deep brain nucleus in a large cohort of healthy individuals or patients usually represents the first step of exploring a brain structure. Approaching to more advanced MRI methods, this can then be built open by studying a brain region’s structural and connectivity through diffusion-weighted and functional MRI, respectively. Accurate and objective segmentation through atlas-based approaches in standard space have contributed a lot in order to make structural brain MRI scans accessible to studies in large cohorts and have consecutively driven forward our understanding of the brain by laying the foundation for further exploration of a structure’s capacities (Aljabar et al., 2009; Ewert et al., 2019).

However, not all anatomically labeled brain structures are amenable to atlas-based segmentation methods and particularly the human claustrum has not been included as a label of MRI atlases of the brain. It may be partly

¹https://github.com/hongweilibran/claustrum_multi_view

due to this fact that our knowledge about this thin and delicate grey matter structure lying subjacent to the insular cortex is still minimal despite intensified research efforts in the last one and a half decades ([Jackson et al., 2020](#)). Studies reproducing the wide structural connectivity of the claustrum found in mice investigating human MRI scans were based on few individuals due to the need for labor-intensive and time-consuming manual segmentations ([Arrigo et al., 2017](#)). Thus, in order to promote our understanding of the human claustrum, an objective and accurate, automated segmentation method, which can be applied to large cohorts is needed.

In recent years, computer vision and machine learning techniques have been increasingly used in the medical field pushing the limits of atlas-based segmentation methods. Especially, deep-learning ([LeCun et al., 2015](#)) based approaches have shown promising results on various medical image segmentation tasks e.g. brain structure and tumor segmentation in MR images ([Chen et al., 2018](#); [Kamnitsas et al., 2017](#); [Wachinger et al., 2018](#); [Prados et al., 2017](#)). Recent segmentation methods commonly rely on so-called convolutional neural networks (CNNs). Applied to segmentation tasks, these networks “learn” proper annotation of any structure from a set of manually labeled data serving as ground truth for training. In the inference stage, CNNs perform the segmentation on previously unseen images, usually much faster and at very high reported accuracies also for tiny structures such as white-matter lesions ([Li et al., 2018](#)) comparing with traditional approaches.

Thus, we hypothesize that deep learning techniques used to segment the claustrum on MR images can fill the currently existing gap. Based on a large number of manually annotated, T1-weighted brain MRI scans, we propose a 2D multi-view framework for fully-automated claustrum segmentation. In order to assess our main hypothesis, we will assess the segmentation accuracy of our algorithm on an annotated dataset using three canonical evaluation metrics and compare it to intra-rater variability. Further, we will investigate whether multi-view information significantly improves the segmentation performance. In addition, we will address the questions of robustness against e.g. scanner type and how increasing the training set impacts segmentation accuracy. We upload it to an open-source repository so that it can be used by researchers worldwide.

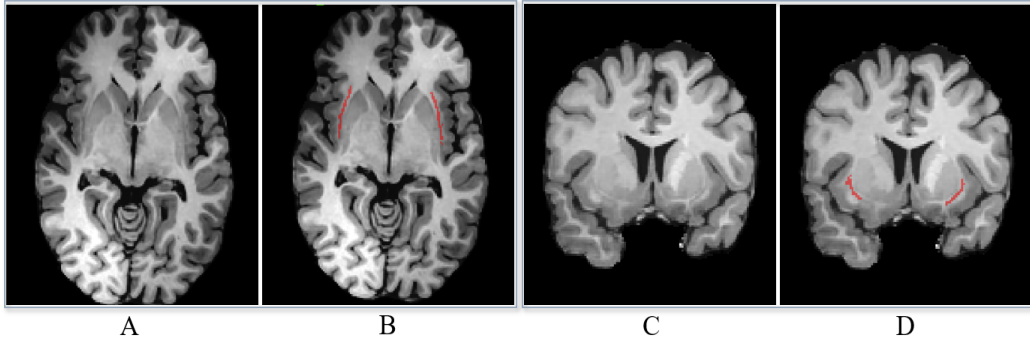


Figure 1: Examples of axial (A, B) and coronal (C, D) MR slices with corresponding manual annotation of the claustrum structure (in B and D) by a neuroradiologist.

2. Materials

This section describes the datasets and evaluation metrics which are referred to in the rest of the article.

2.1. Datasets

T1-weighted three-dimensional scans of 181 individuals were included from the Bavarian Longitudinal Study (Riegel et al., 1995; Wolke and Meyer, 1999). The study was carried out in accordance with the *Declaration of Helsinki* and was approved by the local institutional review boards. Written consent was obtained from all participants. The MRI acquisition took place at two sites: the Department of Neuroradiology, Klinikum rechts der Isar, Technische Universität München (n=120) and the Department of Radiology, University Hospital of Bonn (n=61). MRI examinations were performed at both sites on either a *Philips Achieva 3T* or a *Philips Ingenia 3T* system using an 8-channel SENSE head-coils.

The imaging protocol include a high-resolution T1-weighted, 3D-MPRAGE sequence (TI = 1300ms, TR = 7.7ms, TE = 3.9ms, flip angle 15°; field of view: 256 mm × 256 mm)² with a reconstructed isotropic voxel size of 1 mm³. All images are visually inspected for artifacts and gross brain lesions that could potentially impair manual claustrum segmentation. Prior

²MPRAGE: Magnetization Prepared Rapid Acquisition Gradient Echo; TE: Time to echo; TI: Time to inversion; TR: Time to repetition

Table 1: Characteristics of the dataset in this study. The dataset consists 181 subjects data from four scanners.

Datasets	Scanner Name	Voxel Size (m^3)	Total
Bonn-1	Philips Achieva 3T	1.00×1.00×1.00	15
Bonn-2	Philips Ingenia 3T	1.00×1.00×1.00	46
Munich-1	Philips Achieva 3T	1.00×1.00×1.00	103
Munich-2	Philips Ingenia 3T	1.00×1.00×1.00	17

to manual segmentation, the images are skull-stripped using ROBEX (Iglesias et al., 2011) and image denoising is applied using the spatially-adaptive nonlocal means for 3D MRI filter (Manjón et al., 2010) in order to increase delineability of the claustrum. Manual annotations were performed by a neuroradiologist with 7 years of experience using a modified segmentation protocol from Davis (2008) in ITK-SNAP (Yushkevich et al., 2006).

2.2. Evaluation Metrics and Protocol

Three metrics are used to evaluate the segmentation performance in different aspects in the reported experiments. Given a ground-truth segmentation map G and a predicted segmentation map P generated by an algorithm, the three evaluation metrics are defined as follows.

2.2.1. Volumetric similarity (VS)

Let V_G and V_P be the volume of region of interest in G and P respectively. Then the Volumetric similarity (VS) in percentage is defined as:

$$VS = 1 - \frac{|V_G - V_P|}{V_G + V_P} \quad (1)$$

2.2.2. Hausdorff distance (95th percentile) (HD95)

Hausdorff distance is defined as:

$$H(G, P) = \max\{\sup_{x \in G} \inf_{y \in P} d(x, y), \sup_{y \in P} \inf_{x \in G} d(x, y)\} \quad (2)$$

where $d(x, y)$ denotes the distance of x and y , *sup* denotes the supremum and *inf* for the infimum. This measures the distance between the two subsets of metric space. It is modified to obtain a robust metric by using the 95th percentile instead of the maximum (100th percentile) distance.

2.2.3. Dice similarity coefficient (DSC)

$$DSC = \frac{2(G \cap P)}{|G| + |P|} \quad (3)$$

This measures the overlap in percentage between ground truth maps G and prediction maps P .

We use k-fold cross validation to evaluate the overall performance. In each split, 80% of the scans from *each scanner* are pooled into the training set, and the remaining scans from *each scanner* for testing. This procedure is repeated until all of the subjects were used in testing phase.

3. Methods

3.1. Advanced Preprocessing

An additional preprocessing step is performed on top of the basic preprocessing steps carried out by the rater (Section 2.1). Indeed we normalize the voxel intensities to reduce the variations across subjects and scanners, thus a simple yet effective preprocessing step is used in both training and inference stages. It includes two steps: 1) cropping or padding each slice to a uniform size and 2) z -score normalization of the brain voxel intensities. All the axial and coronal slices are automatically cropped or padded to 180×180 , to guarantee a uniform input size for the deep-learning model. The z -score normalization is performed for individual 3D scan, including two steps. Firstly, a 3D brain mask is obtained by a simple thresholding and morphology operations. Then the mean and standard deviation are calculated based on the intensities *within* each individual’s brain mask. Finally the voxel intensities are rescaled to zero mean and unit standard deviation.

3.2. Multi-View Fully Convolutional Neural Networks

3.2.1. Multi-View Learning

The imaging appearance of the claustrum is low in contrast and its structure is very tiny. Neuroradiologists rely on axial and coronal views to identify the structure when performing manual annotations. Thus we hypothesize that the image features from the two geometric views would be complementary to locate the claustrum and would be beneficial for reducing false positives on individual views. We train two individual deep CNN models on 2D single-view slices after parsing 3D MRI volume into axial and coronal

views. The sagittal view is excluded because we find it does not improve segmentation results - it will be discussed in Section 4.2. We propose a simple and effective approach to aggregate the multi-view information in probability space in voxel-wise level during the inference stage.

Let $f_a(x)$ and $f_c(x)$ be the single-view models trained on the 2D image slices from axial and coronal views respectively. During the testing stage, given an image volume (scan) $V \in \mathbb{R}^{d_1, d_2, d_3}$, it is transposed to the axial space and coronal space $V_a \in \mathbb{R}^{w_a, h_a, n_a}$ and $V_c \in \mathbb{R}^{w_c, h_c, n_c}$ by function T_a and T_c respectively, where w_a , w_c , n_a and h_a , h_c , n_c are the widths, heights and number of the axial and coronal slices respectively. Let P_a and P_c be the segmentation maps in volumes predicted by $f_a(x)$ and $f_c(x)$ respectively. We fuse the multi-view information by averaging the voxel-wise probabilities generated by single-view models. The final segmentation masks in volume after ensemble is define as:

$$P_F = \frac{1}{2}(\lambda T_a^{-1}(P_a) + (1 - \lambda)T_c^{-1}(P_c)) \quad (4)$$

where T_a^{-1} and T_c^{-1} are the inverse axis-transformation functions of T_a and T_c respectively. λ is used to balance the contribution of each view and it is set to 0.5 in the experiments.

3.2.2. Single-View 2D Convolutional Network Architecture

We build a 2D architecture based on a recent U-Net (Ronneberger et al., 2015; Li et al., 2018) and tailored for the claustrum segmentation. The network architecture is delineated in Figure 2. It consists of a down-convolutional part that shrinks the spatial dimensions (left side), and up-convolutional part that expands the score maps (right side). The skip connections between down-convolutional and up-convolutional are used. In this model, two convolutional layers are repeatedly employed, each followed by a rectified linear unit (ReLU) and a 2×2 max pooling operation with stride 2 for downsampling. At the final layer a 1×1 convolution is used to map each 64-component feature vector to two classes. In total the network contains 16 convolutional layers. The network takes the single-view slices of T1 modality scans as the input during both training and testing.

3.2.3. Loss Function

In the task of claustrum segmentation, the numbers of positives (claustrum) and negatives (non-claustrum) are highly unbalanced. One of the

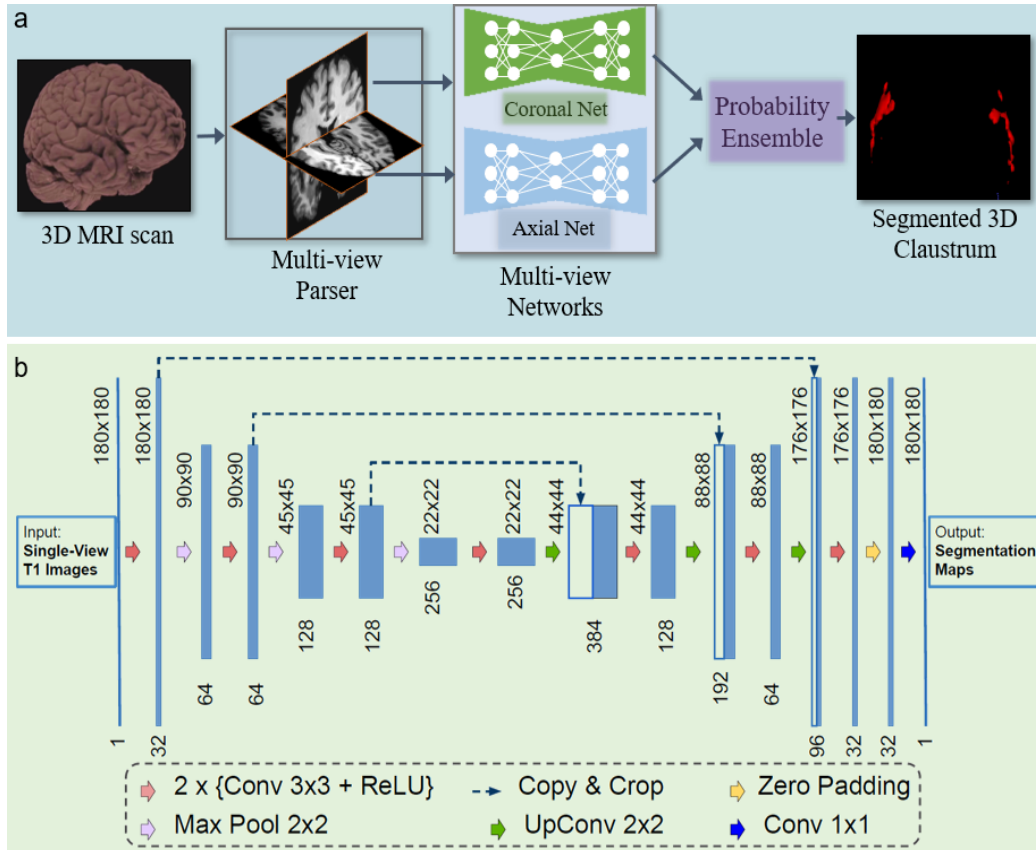


Figure 2: a) A schematic view of the proposed segmentation system using multi-view fully convolutional networks to jointly segment the claustrum; b) 2D Convolutional network architecture for each view (i.e. axial and coronal). It takes the raw images as the input and predicts its segmentation maps. The network consists of several non-linear computational layers in a shrinking part (left side) and an expansive part (right side) to extract semantic features of the claustrum structure.

promising solutions to tackle this issue is to use Dice loss (Milletari et al., 2016) as the loss function for training the model. The formulation is as follows.

Let $G = \{g_1, \dots, g_N\}$ be the ground-truth segmentation maps over N slices, and $P = \{p_1, \dots, p_N\}$ be the predicted probabilistic maps over N slices. The Dice loss function can be expressed as:

$$DL = -\frac{2 \sum_{n=1}^N |p_n \circ g_n| + s}{\sum_{n=1}^N (|p_n| + |g_n|) + s} \quad (5)$$

where \circ represents the entrywise product of two matrices, and $|\cdot|$ represents the sum of the matrix entries. The s term is used here to ensure the loss function stability by avoiding the division by 0, i.e., in a case where the entries of G and P are all zeros. s is set to 1 in our experiments.

3.3. Anatomically Consistent Post-Processing

The post-processing for the 3D segmentation result included two aspects: 1) cropping or padding the segmentation maps with respect to the original size, i.e., an inverse operation to the step described in Section 3.1; 2) removing some anatomically unreasonable artefact in the slices. For the purpose of removing unreasonable detections (e.g., the claustrum does not appear in the first and last slices which contain skull or other tissues), we employed a simple strategy: if there is a claustrum structure detected in the first m and last n ones of a brain along the z -direction, they are considered as false positives. Empirically, m and n are set to 20% of the number of axial slices for each scan. The codes and models of the proposed method are made publicly available in *GitHub*³.

3.4. Parameter Setting and Computation Complexity

An appropriate parameter setting is crucial to the successful training of deep convolutional neural networks. We selected the number of epochs to stop the training by contrasting training loss and the performance on validation set over epochs in each experiment as shown in Figure S2 in Supplement. Hence we choose a number of N epochs to avoid over fitting by observing the VS and DSC on a validation set, and to keep a low computational cost. The batch size was empirically set to 30 and the learning rate was set to 0.0002

³https://github.com/hongweilibran/claustrum_multi_view

throughout all of the experiments by observing the training stability on the validation set.

All of the experiments are conducted on a GNU/Linux server running Ubuntu 18.04, with 64GB RAM memory. The number of trainable parameters in the proposed model with one-channel inputs (T1) is 4,641,209. The algorithms were trained on a single NVIDIA Titan-V GPU with 12GB RAM memory. It takes around 100 minutes to train a single model for 200 epochs on a training set containing 5,000 images of size 180×180 each. For testing, the segmentation of one scan with 192 slices by an ensemble of two models takes around 90 seconds using an Intel Xeon CPU (E3-1225v3) (without the use of GPU). In contrast, the segmentation per scan takes only 6 seconds when using a GPU.

4. Results

4.1. Manual Segmentation: Intra-rater Variability

In order to set a benchmark accuracy for manual segmentation, intra-rater variability was assessed based on repeated annotations of 20 left and right claustrums by the same experienced neuroradiologist. In order to assure independent segmentation, annotations were performed at least three months apart. We obtained the intra-rater variability on 20 scans using the metrics VS, DSC, and HD95 and report the following median values with interquartile ranges (IQR): VS: 0.949, [0.928, 0.972]; DSC: 0.667, [0.642, 0.704], HD95: 2.24 mm, [2.0, 2.55].

4.2. AI-based segmentation: Single-view vs. Multi-view

In order to investigate the added value of multi-view information for the proposed system, we compare the segmentation performances of single-view model (i.e. axial, coronal or sagittal) and multi-view ensemble model. To exclude the influence of scanner acquisition, we evaluate our method on the data from one scanner (*Munich-Ingénia*) including 103 subjects and perform five-fold cross validation for fair comparison. In each split, the single-view CNNs and multi-view CNNs ensemble model are trained on same subjects, and are evaluated on the test cases with respect to the three evaluation metrics. Table 2 shows the segmentation performance of each setting. We observed that sagittal view yields the worse performance among the three views. In manual annotation practice it is much more challenging to distinguish the claustrum from sagittal view than from axial and coronal views.

Table 2: Segmentation performances (median values) of the single-view approaches and multi-view approaches. The combination of axial and coronal views shows its superiority over individual views. Note that we used equal weights for each view in the multi-view ensemble model. ↓ indicates that smaller value represents better performance. (VS=volumetric similarity, HD95=95th percentile of Hausdorff Distance, DSC=Dice similarity coefficient)

Metrics	Axial (A)	Coronal (C)	Sagittal (S)	A+C	A+C+S	p-value		
						A+C <i>vs.</i> A	A+C <i>vs.</i> C	A+C <i>vs.</i> A+C+S
VS (%)	94.4	94.7	79.1	93.3	92.9	0.636	0.008	0.231
HD95 (mm)↓	1.73	1.41	3.21	1.41	1.73	<0.001	<0.001	0.035
DSC (%)	69.7	70.0	55.2	71.8	71.0	<0.001	<0.001	0.021

We further perform statistical analysis (Wilcoxon signed rank test) , to compare the statistical significance between the proposed *single-view* CNNs and *multi-view* CNNs ensemble model. We observed that the improvement achieved by two-view (axial+coronal) approach over single-view ones, are significant on H95 and DSC. We further compared the three-view approach with the two-view one which excludes sagittal view, and found that they are comparable in terms of VS, and the two-view approach outperforms three-view ones in terms of HD95 ($p = 0.035$) and DSC ($p = 0.021$).

In the following sections, we use the *axial+coronal* setting to perform segmentation and evaluate the method.

4.3. AI-based Segmentation: Stratified K-fold Cross Validation

In order to evaluate the general performance of our method on the whole dataset, we performed stratified five-fold cross validation. In each fold, we take 80% subjects from each scanner and pool them into a training set, and use the rest as a test set. This procedure is repeated until all the scanners are used as test set. Figure 3 and Table 3 shows the segmentation performance of three metrics on 181 scans from four scanners, showing its effectiveness with respect to volume measurements and localization accuracy. In order to compare AI-based segmentation performance to the human expert rater benchmark performance, we performed Mann-Whitney U testing of the three metrics (see Table 3). We found no statistical difference between manual and AI-based segmentation with respect to VS and superior performance of AI-based segmentation with respect to HD95 and Dice score. This indicates that AI-based segmentation performance equal of superior to human expert level.

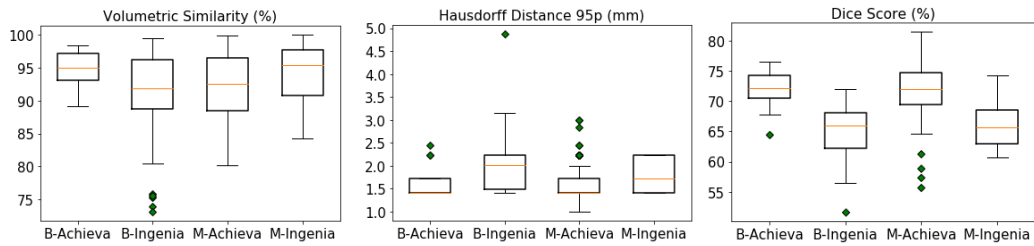


Figure 3: Results of five-fold cross validation on the 181 scans across four scanners: *Bonn-Achieva*, *Bonn-Ingenia*, *Munich-Achieva* and *Munich-Ingenia*. Each box plot summarizes the segmentation performance from one scanner using one specific metric.

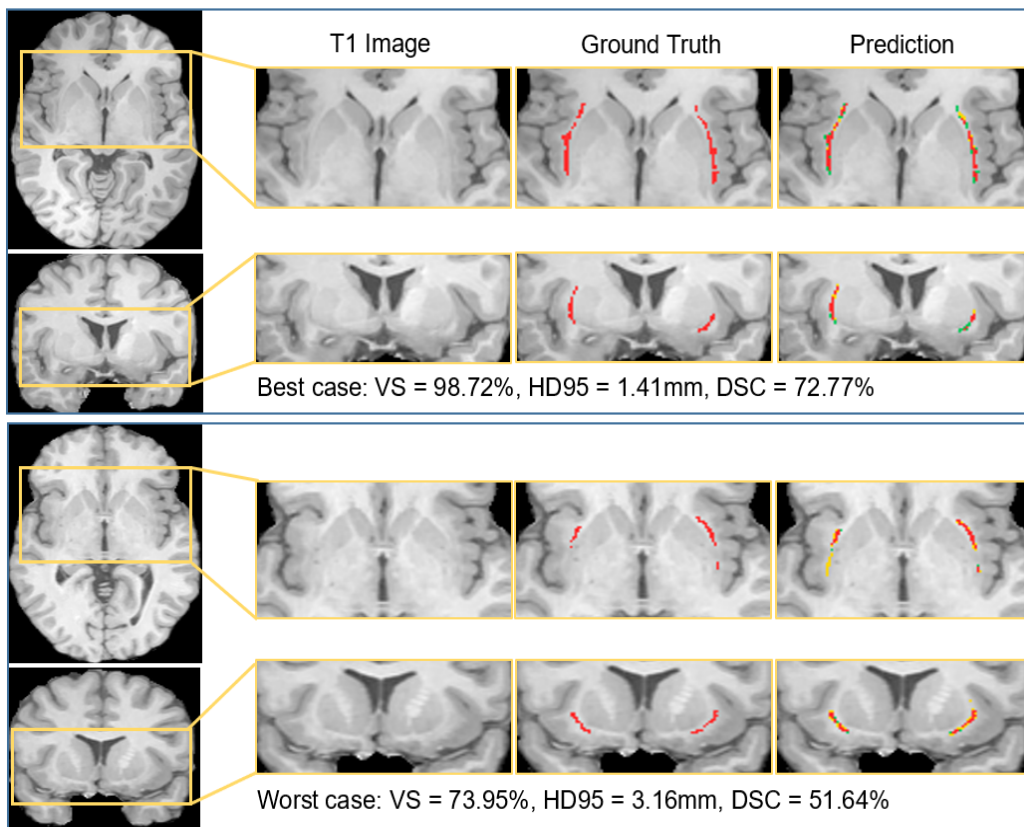


Figure 4: Segmentation results of the best case and the worst case. In the prediction maps, the red pixels represent true positives, the green ones represent false negatives, and yellow ones represent false positives.

Table 3: Performance comparison of manual and AI-based segmentations. \downarrow indicates that smaller value represents better performance. HD95=95th percentile of Hausdorff Distance.

Metrics	Manual segmentation [Median, IQR]	AI-based segmentation [Median, IQR]	p-value
Volumetric similarity (%)	94.9, [0.928, 0.972]	93.3, [89.2, 96.7]	0.095
HD95 (mm) \downarrow	2.24, [2.0, 2.55]	1.41, [1.41, 2.24]	< 0.001
Dice score (%)	66.7, [0.642, 0.704]	71.8, [66.3, 73.4]	0.012

4.4. AI-based Segmentation: Influence of Individual scanners

To evaluate the generalizability of our method to unseen scanners, we present a leave-one-scanner-out study. For the cross-scanner analysis, we use the scanner IDs to split the 181 cases into training and test sets. In each split, the subjects from three scanners are used as training set while the subjects from the remaining scanner are used for a test set. This procedure is repeated until all the scanners are used as test set. The achieved performance is comparable with the cross-validation results in Section 4.3 where all scanners were seen in the training set. Figure 5 plots the distributions of segmentation performances on four scanners being tested in turns. We further perform statistical analysis (i.e. Wilcoxon rank-sum tests) to compare it with the result in Section 4.3. As shown in Table 4, we found that the cross-validation results achieved significant lower HD95 and higher DSC than leave-one-scanner-out results and they are comparable in terms of VS. This is because the former evaluation sees all the scanners in the training stage thus do not suffer from domain shift. We found statistical difference between them with respect to HD95 and Dice score. This indicates that the unseen scanners cause a negative effect on the segmentation performance.

To further investigate the influence of scanner acquisition for segmentation, we individually perform five-fold cross validation on the sub-sets *Bonn-Ingenia* and *Munich-Achieva* using subject IDs. The other two scanners are not evaluated because they contain relatively fewer scans. We use Mann-Whitney U test to compare the performance of two groups. we found that *Bonn-Ingenia* obtained significantly higher VS and higher DSC than *Munich-Achieva*. This indicates that scanner characteristics such as image contrast, noise level, etc., generally affect the performance of AI-based segmentation. The box plots of the two evaluations are in Figure S1 in Supplement.

Table 4: Results and statistics analysis of leave-one-scanner-out segmentation results and k-fold cross-validation results. \downarrow indicates that smaller value represents better performance. HD95=95th percentile of Hausdorff Distance.

Metrics	Leave-one-scanner-out [Median, IQR]	k-fold cross-validation [Median, IQR]	p-value
Volumetric similarity (%)	93.0, [89.1, 96.6]	93.3, [89.2, 96.7]	0.268
HD95 (mm) \downarrow	1.73, [1.41, 2.24]	1.41, [1.41, 2.24]	< 0.001
Dice score (%)	69.1, [65.3, 71.7]	71.8, [66.3, 73.4]	< 0.001

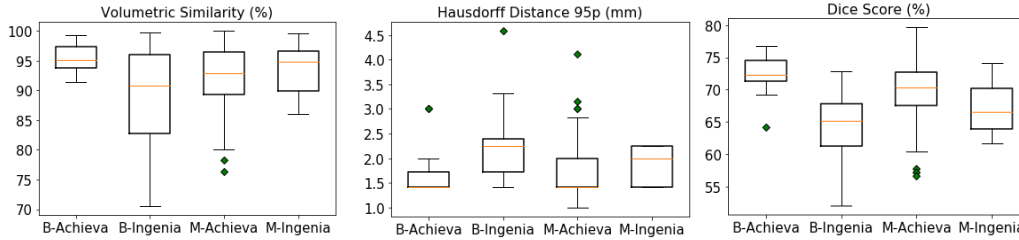


Figure 5: Results of leave-one-scanner-out evaluation on the four scanners. Each box plot summarizes the segmentation performance on subject from four testing scanners using one specific metric. For example, for box plot scanner 1 (*Bonn-Achieva*) in the upper left figure, it shows the distribution of segmentation results on scanner 1 when training the model by using data from three other scanners.

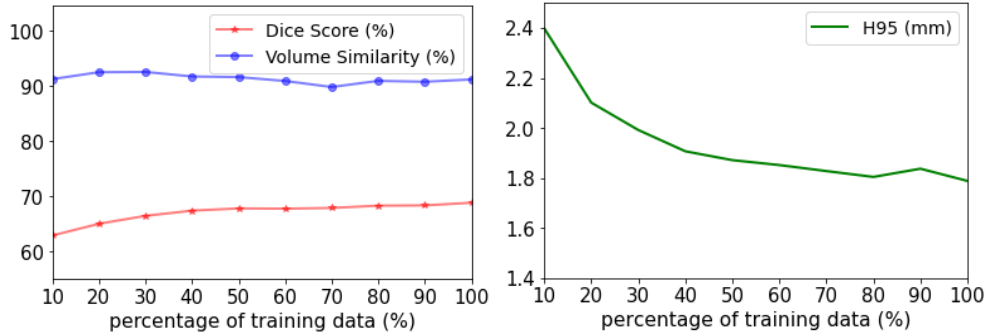


Figure 6: Segmentation performance on the validation set when gradually increasing the percentage of the training data by a step of 10%.

4.5. How Much Training Data Is Needed?

Since supervised deep learning is a data-driven machine learning method, it commonly requires a large amount of training data to optimize the non-linear computational model. However, it is necessary to know the bound when model begins to saturate because manual annotation is expensive. Here, we perform a quantitative analysis on the effect of the amount of training data. Specifically, we split the 181 scans into a training set and a validation set with a ratio of 4:1 in a stratified manner from 4 scanners, resulting in 146 subjects for training and 35 for validation. As a start, we randomly pick 10% of the scans from the training set, train and test the model. Then we gradually increased the size of the training set by a step of 10%. Figure 6 shows that the HD95 and the DSC only marginally improve on the validation set - when $> 50\%$ of the training set is used, while the VS is rather stable over the whole range. Thus we conclude that a training set including around 75 scans and annotations is sufficient to obtain a good segmentation result.

5. Discussion

We have presented a deep-learning based approach to accurately segment the claustrum, a complex grey matter structure of the human forebrain which so far has not been amenable to atlas-based segmentation. The proposed method uses multi-view information from T1-weighted MRI and achieves expert-level segmentation in a fully automated manner. To the best of our

knowledge, this is the first work on fully automated segmentation of human claustrum using state-of-the-art deep learning techniques.

The first finding is that the segmentation performance benefits from leveraging multi-view information, specifically from combining axial and coronal orientations. The significance of improvement was confirmed using paired difference tests. The multi-view fusion process imitates the annotation workflow by neuroradiologists, which relies on 3D anatomical knowledge from multiple views. This strategy is also shown to be effective in common brain structure segmentation (Zhao et al., 2019; Wei et al., 2019) and cardiac image segmentation (Chen et al., 2020; Mortazi et al., 2017). We observed that integrating sagittal view is not helpful for boosting the performance. This is due to the fact that the claustrum, a thin, sheet-like is mainly oriented sagittal plane and thus can be hardly delineated in sagittal view.

The proposed method yields a high median volumetric similarity, a small Hausdorff distance and Dice score of 93.3%, 1.41mm and 71.8% respectively in the cross-validation experiments. Although the achieved Dice score presents relatively small value, we claim that this is excellent considering the structure of the claustrum is very tiny (normally less than 1500 voxels). We illustrate the correlation between Dice scores and claustrum volumes in Supplement. In similar tasks such as segmentation of multiple sclerosis lesions with thousands of voxels, Dice score around 75% would be considered excellent. For the segmentation of larger tissues such as white matter and grey matter, Dice scores would reach 95% (Gabr et al., 2019). Nevertheless, HD95 which quantifies the distance between prediction and ground-truth masks, is a robust metric to assess very small and thin structures (Kuijf et al., 2019).

Another valuable finding is that the proposed algorithm achieves expert-level segmentation performance and even outperforms human rater in terms of DSC and HD95. This is confirmed by comparing the two groups of segmentation performances done by human rater and the proposed method. We conclude that the human rater presents more bias when the structure is tiny and ambiguous while AI-based algorithm basically learns to fit the available knowledge and shows a stable behaviour when doing the inference. This finding is in line with recent advances in biomedical research where deep learning based methods demonstrate unbiased quantification of structures (Todorov et al., 2019). The proposed method would allow us to quantify the complex grey matter structure in an accurate and unbiased manner.

We found that the segmentation performance slightly dropped when the AI-based model was tested on unseen scanners. This is common observed

in machine learning tasks caused by the domain shift (Glocker et al., 2019) between training and testing data that are with different distributions. From our observation, the performance drop in the experiment is not severe and the segmentation outcome is satisfactory. This is due to the fact that scanners are in similar resolution, from the same manufacturer and the scans are properly pre-processed, resulting in a small domain gap. To enforce our model to be generalized to unseen scanners from different manufactures and resolutions, domain adaptation methods (Kamnitsas et al., 2017; Dou et al., 2019) are to be investigated in future studies.

Although the proposed method reaches expert-level performance and provide unbiased quantification results, there are a few limitations in our work. First, the human claustrum has a very thin and sheet-like structure. Thus, also high resolution imaging as used in this study at an isotropic resolution of 1 mm^3 will result in partial volume effects which significantly affects both the manual expert annotation as well as the automated segmentation. We addressed this bias by using a clear segmentation protocol in order to reduce variability in manual annotations used as the reference standard. Second, the data distribution of the four datasets are highly imbalanced. It potentially affects the accuracy of leave-one-scanner-out experiment in Section 4.4 especially when a large sub-set (e.g. Munich-2) was taken out as a test set. In future work, evaluating the scanner influence on a more balanced dataset would avoid such an effect.

6. Conclusions

In this paper we described in detail a multi-view deep learning approach for automatic segmentation of human claustrum structure. We empirically studied the effectiveness of multi-view information, the influence of imaging protocols as well as the effect of the amount of training data. We found that: 1) multi-view information including coronal and axial views provide complementary information to identify the claustrum structure; 2) multi-view automatic segmentation is superior to manual segmentation accuracy; 3) scanner type influence segmentation accuracy even for identical sequence parameter settings; 4) a training set with 75 scans and annotation is sufficient to achieve satisfactory segmentation result. We have made our *Python* implementation codes available on *GitHub* to the research community.

Acknowledgment

We thank all current and former members of the Bavarian Longitudinal Study Group who contributed to general study organization, recruitment, and data collection, management and subsequent analyses, including (in alphabetical order): Barbara Busch, Stephan Czeschka, Claudia Grünzinger, Christian Koch, Diana Kurze, Sonja Perk, Andrea Schreier, Antje Strasser, Julia Trummer, and Eva van Rossum. We are grateful to the staff of the Department of Neuroradiology in Munich and the Department of Radiology in Bonn for their help in data collection. Most importantly, we thank all our study participants and their families for their efforts to take part in this study. This study is supported by the Deutsche Forschungsgemeinschaft (SO 1336/1-1 to C.S.), German Federal Ministry of Education and Science (BMBF 01ER0801 to P.B. and D.W., BMBF 01ER0803 to C.S.) and the Kommission für Klinische Forschung, Technische Universität München (KKF 8765162 to C.S). We also thank NVIDIA for the donation of a GeForce graphic card. The authors declare no conflict of interest.

References

- S. B. Eickhoff, B. T. Yeo, S. Genon, Imaging-based parcellations of the human brain, *Nature Reviews Neuroscience* 19 (2018) 672–686.
- A. Arrigo, E. Mormina, A. Calamuneri, M. Gaeta, F. Granata, S. Marino, G. Anastasi, D. Milardi, A. Quartarone, Inter-hemispheric claustral connections in human brain: a constrained spherical deconvolution-based study, *Clinical neuroradiology* 27 (2017) 275–281.
- J. D. Bijsterbosch, M. W. Woolrich, M. F. Glasser, E. C. Robinson, C. F. Beckmann, D. C. Van Essen, S. J. Harrison, S. M. Smith, The relationship between spatial configuration and functional connectivity of brain regions, *Elife* 7 (2018) e32992.
- R. S. Desikan, F. Ségonne, B. Fischl, B. T. Quinn, B. C. Dickerson, D. Blacker, R. L. Buckner, A. M. Dale, R. P. Maguire, B. T. Hyman, et al., An automated labeling system for subdividing the human cerebral cortex on mri scans into gyral based regions of interest, *Neuroimage* 31 (2006) 968–980.

- N. Makris, J. M. Goldstein, D. Kennedy, S. M. Hodge, V. S. Caviness, S. V. Faraone, M. T. Tsuang, L. J. Seidman, Decreased volume of left and total anterior insular lobule in schizophrenia, *Schizophrenia research* 83 (2006) 155–171.
- J. A. Frazier, S. Chiu, J. L. Breeze, N. Makris, N. Lange, D. N. Kennedy, M. R. Herbert, E. K. Bent, V. K. Koneru, M. E. Dieterich, et al., Structural brain magnetic resonance imaging of limbic and thalamic volumes in pediatric bipolar disorder, *American Journal of Psychiatry* 162 (2005) 1256–1265.
- M. Goodkind, S. B. Eickhoff, D. J. Oathes, Y. Jiang, A. Chang, L. B. Jones-Hagata, B. N. Ortega, Y. V. Zaiko, E. L. Roach, M. S. Korgaonkar, et al., Identification of a common neurobiological substrate for mental illness, *JAMA psychiatry* 72 (2015) 305–315.
- M. F. Glasser, T. S. Coalson, E. C. Robinson, C. D. Hacker, J. Harwell, E. Yacoub, K. Ugurbil, J. Andersson, C. F. Beckmann, M. Jenkinson, et al., A multi-modal parcellation of human cerebral cortex, *Nature* 536 (2016) 171–178.
- P. Aljabar, R. A. Heckemann, A. Hammers, J. V. Hajnal, D. Rueckert, Multi-atlas based segmentation of brain images: atlas selection and its effect on accuracy, *Neuroimage* 46 (2009) 726–738.
- S. Ewert, A. Horn, F. Finkel, N. Li, A. A. Kühn, T. M. Herrington, Optimization and comparative evaluation of nonlinear deformation algorithms for atlas-based segmentation of dbs target nuclei, *NeuroImage* 184 (2019) 586–598.
- J. Jackson, J. B. Smith, A. K. Lee, The anatomy and physiology of claustrum-cortex interactions, *Annual Review of Neuroscience* 43 (2020).
- Y. LeCun, Y. Bengio, G. Hinton, Deep learning, *nature* 521 (2015) 436.
- H. Chen, Q. Dou, L. Yu, J. Qin, P.-A. Heng, Voxresnet: Deep voxelwise residual networks for brain segmentation from 3d mr images, *NeuroImage* 170 (2018) 446–455.
- K. Kamnitsas, C. Ledig, V. F. Newcombe, J. P. Simpson, A. D. Kane, D. K. Menon, D. Rueckert, B. Glocker, Efficient multi-scale 3d cnn with fully

- connected crf for accurate brain lesion segmentation, *Medical image analysis* 36 (2017) 61–78.
- C. Wachinger, M. Reuter, T. Klein, Deepnat: Deep convolutional neural network for segmenting neuroanatomy, *NeuroImage* 170 (2018) 434–445.
- F. Prados, J. Ashburner, C. Blaiotta, T. Brosch, J. Carballido-Gamio, M. J. Cardoso, B. N. Conrad, E. Datta, G. Dávid, B. De Leener, et al., Spinal cord grey matter segmentation challenge, *Neuroimage* 152 (2017) 312–329.
- H. Li, G. Jiang, J. Zhang, R. Wang, Z. Wang, W.-S. Zheng, B. Menze, Fully convolutional network ensembles for white matter hyperintensities segmentation in mr images, *NeuroImage* 183 (2018) 650–665.
- K. Riegel, B. Orth, D. Cloud, K. Osterlund, Development of born children up to 5, age. Enke, Stuttgart (1995).
- D. Wolke, R. Meyer, Cognitive status, language attainment, and prereading skills of 6-year-old very preterm children and their peers: the bavarian longitudinal study, *Developmental medicine and child neurology* 41 (1999) 94–109.
- J. E. Iglesias, C.-Y. Liu, P. M. Thompson, Z. Tu, Robust brain extraction across datasets and comparison with publicly available methods, *IEEE transactions on medical imaging* 30 (2011) 1617–1634.
- J. V. Manjón, P. Coupé, L. Martí-Bonmatí, D. L. Collins, M. Robles, Adaptive non-local means denoising of mr images with spatially varying noise levels, *Journal of Magnetic Resonance Imaging* 31 (2010) 192–203.
- W. G. Davis, The claustrum in autism and typically developing male children: a quantitative mri study (2008).
- P. A. Yushkevich, J. Piven, H. C. Hazlett, R. G. Smith, S. Ho, J. C. Gee, G. Gerig, User-guided 3d active contour segmentation of anatomical structures: significantly improved efficiency and reliability, *Neuroimage* 31 (2006) 1116–1128.
- O. Ronneberger, P. Fischer, T. Brox, U-net: Convolutional networks for biomedical image segmentation, in: *International Conference on Medical Image Computing and Computer-Assisted Intervention*, Springer, 2015, pp. 234–241.

- F. Milletari, N. Navab, S.-A. Ahmadi, V-net: Fully convolutional neural networks for volumetric medical image segmentation, in: 3D Vision (3DV), 2016 Fourth International Conference on, IEEE, 2016, pp. 565–571.
- Y.-X. Zhao, Y.-M. Zhang, M. Song, C.-L. Liu, Multi-view semi-supervised 3d whole brain segmentation with a self-ensemble network, in: International Conference on Medical Image Computing and Computer-Assisted Intervention, Springer, 2019, pp. 256–265.
- J. Wei, Y. Xia, Y. Zhang, M3net: A multi-model, multi-size, and multi-view deep neural network for brain magnetic resonance image segmentation, *Pattern Recognition* 91 (2019) 366–378.
- C. Chen, C. Qin, H. Qiu, G. Tarroni, J. Duan, W. Bai, D. Rueckert, Deep learning for cardiac image segmentation: A review, *Frontiers in Cardiovascular Medicine* 7 (2020) 25.
- A. Mortazi, R. Karim, K. Rhode, J. Burt, U. Bagci, Cardiacnet: segmentation of left atrium and proximal pulmonary veins from mri using multi-view cnn, in: International Conference on Medical Image Computing and Computer-Assisted Intervention, Springer, 2017, pp. 377–385.
- R. E. Gabr, I. Coronado, M. Robinson, S. J. Sujit, S. Datta, X. Sun, W. J. Allen, F. D. Lublin, J. S. Wolinsky, P. A. Narayana, Brain and lesion segmentation in multiple sclerosis using fully convolutional neural networks: A large-scale study, *Multiple Sclerosis Journal* (2019) 1352458519856843.
- H. J. Kuijf, J. M. Biesbroek, J. De Bresser, R. Heinen, S. Andermatt, M. Bento, M. Berseth, M. Belyaev, M. J. Cardoso, A. Casamitjana, et al., Standardized assessment of automatic segmentation of white matter hyperintensities and results of the wmh segmentation challenge, *IEEE transactions on medical imaging* 38 (2019) 2556–2568.
- M. I. Todorov, J. C. Paetzold, O. Schoppe, G. Tetteh, V. Efremov, K. Völgyi, M. Düring, M. Dichgans, M. Piraud, B. Menze, et al., Automated analysis of whole brain vasculature using machine learning, *bioRxiv* (2019) 613257.
- B. Glocker, R. Robinson, D. C. Castro, Q. Dou, E. Konukoglu, Machine learning with multi-site imaging data: An empirical study on the impact of scanner effects, *arXiv preprint arXiv:1910.04597* (2019).

- K. Kamnitsas, C. Baumgartner, C. Ledig, V. Newcombe, J. Simpson, A. Kane, D. Menon, A. Nori, A. Criminisi, D. Rueckert, et al., Unsupervised domain adaptation in brain lesion segmentation with adversarial networks, in: International conference on information processing in medical imaging, Springer, 2017, pp. 597–609.
- Q. Dou, D. C. de Castro, K. Kamnitsas, B. Glocker, Domain generalization via model-agnostic learning of semantic features, in: Advances in Neural Information Processing Systems, 2019, pp. 6447–6458.